atmosphere

MDPI

Article

The Design of a Parameterization Scheme for ^{137}Cs Based on the WRF-Chem Model and Its Application in Simulating the Fukushima Nuclear Accident

Qun Long [1,2], Zengliang Zang [2,3,*], Xiaoyan Ma [1,*], Sheng Fang [4], Yiwen Hu [2], Yijie Wang [2], Shuhan Zhuang [4] and Liang Wang [5]

1 Key Laboratory for Aerosol-Cloud Precipitation of China Meteorological Administration, Nanjing University of Information Science and Technology, Nanjing 210044, China; 20211203022@nuist.edu.cn
2 College of Meteorology and Oceanography, National University of Defense Technology, Changsha 410073, China; 20191103004@nuist.edu.cn (Y.H.); 20211205013@nuist.edu.cn (Y.W.)
3 High Impact Weather Key Laboratory of China Meteorological Administration, Changsha 410073, China
4 Institute of Nuclear and New Energy Technology, Tsinghua University, Beijing 100084, China; fangsheng@tsinghua.edu.cn (S.F.); shuhanzhuang@tsinghua.edu.cn (S.Z.)
5 The 31153 Unit of the Peoples' Liberation Army of China, Nanjing 210016, China; 20211203018@nuist.edu.cn
* Correspondence: zangzengliang@nudt.edu.cn (Z.Z.); xma@nuist.edu.cn (X.M.)

Abstract: Based on the Weather Research and Forecasting Model Coupled with Chemistry (WRF-Chem) atmospheric chemistry model, a parameterization scheme for the radioactive isotope caesium (^{137}Cs), considering processes such as advection, turbulent diffusion, dry deposition, and wet deposition, was constructed, enabling the spatial distribution simulation of the concentration and deposition of ^{137}Cs. The experimental simulation studies were carried out during the high emission period of the Fukushima nuclear accident (from 11 to 17 March 2011). Two sets of comparison experiments, with or without deposition, were designed, the effects of wind field and precipitation on the spatial transport and ground deposition of ^{137}Cs were analyzed, and the influence of wind field and precipitation on ^{137}Cs vertical transport was analyzed in detail. The results indicate that the model can accurately simulate the meteorological and ^{137}Cs variables. On 15 March, ^{137}Cs dispersed towards the Kanto Plain in Japan under the influence of northeastern winds. In comparison to the experiment without deposition, the concentration of ^{137}Cs in the Fukushima area decreased by approximately 286 Bq·m^{-3} in the deposition experiment. Under the influence of updrafts in the non-deposition experiment, a ^{137}Cs cloud spread upward to a maximum height of 6 km, whereas in the deposition experiment, the highest dispersion of the ^{137}Cs cloud only reach a height of 4 km. Affected by the wind field, dry deposition is mainly distributed in Fukushima, the Kanto Plain, and their eastern ocean areas, with a maximum dry deposition of 5004.5 kBq·m^{-2}. Wet deposition is mainly influenced by the wind field and precipitation, distributed in the surrounding areas of Fukushima, with a maximum wet deposition of 725.3 kBq·m^{-2}. The single-station test results from the deposition experiment were better than those for the non-deposition experiment: the percentage deviations of the Tokyo, Chiba, Maebashi, and Naraha stations decreased by 61%, 69%, 46%, and 51%, respectively, and the percentage root mean square error decreased by 46%, 25%, 38%, and 48%, respectively.

Keywords: Fukushima nuclear accident; radionuclides; WRF-Chem model; atmospheric transport; ground deposition

Citation: Long, Q.; Zang, Z.; Ma, X.; Fang, S.; Hu, Y.; Wang, Y.; Zhuang, S.; Wang, L. The Design of a Parameterization Scheme for ^{137}Cs Based on the WRF-Chem Model and Its Application in Simulating the Fukushima Nuclear Accident. *Atmosphere* **2024**, *15*, 646. https://doi.org/10.3390/atmos15060646

Academic Editor: Jimy Dudhia

Received: 11 March 2024
Revised: 29 April 2024
Accepted: 8 May 2024
Published: 28 May 2024

1. Introduction

Nuclear pollution primarily originates from the proliferation of large quantities of radionuclides caused by nuclear explosions or leaks. Common radionuclides, including caesium (^{137}Cs), uranium (^{235}U), xenon (^{133}Xe), iodine (^{131}I), and radium (^{226}Ra), are mainly transported and deposited in the atmosphere as aerosols and gaseous pollutants, posing

serious hazards to the ecological environment and human health, both locally and globally. The strong earthquake and tsunami off the northern coast of Japan on 11 March 2011 [1] led to a major nuclear accident at the Fukushima Daiichi Nuclear Power Plant (FDNPP) in Japan, where large quantities of radionuclides, such as ^{137}Cs, ^{131}I, ^{133}Xe, and ^{235}U, were released into the atmosphere and rapidly dispersed by atmospheric transport [2]. Approximately 7 h after the nuclear accident, a concentration of 577 Bq·m^{-3} of ^{137}Cs was detected at an observation site about 25 km north of Fukushima [3], and subsequently, high radionuclide concentrations were detected in the Americas [4–6], Europe [7], and Asia [8–14], where high radionuclide concentrations were monitored. Therefore, it is of great significance to carry out research on the forecasting and early warning of radionuclides in order to implement safety precautions, emergency responses, and disaster assessment regarding nuclear contamination.

The atmospheric dispersion model is an important method for studying the characteristics of the spatial and temporal distribution of pollutants and for improving air quality forecasting. The prediction of nuclear pollutants is similar to that of general pollutants, and the processes of the advection, turbulence, emission, and deposition of radionuclides in the atmosphere can be predicted by atmospheric dispersion models [15]. The main models current in use include the Gaussian, Lagrangian, and Eulerian theories [16,17]. The Gaussian model is suitable for local-scale (below 20 km) simulations [18], and it is the core module of the standard analysis tools for nuclear power plants, such as ARCON and MACCS, and is also the main model for early nuclear contamination dispersion prediction and nuclear emergency response. However, the Gaussian model is poorly applicable to a wide range of complex meteorological conditions, and it is not capable of describing in detail the deposition and dispersion of pollutants [19–22]. The Lagrangian model, which follows the coordinate system of object motion to describe the pollutant concentration and its changes, is applicable to the prediction of nuclear contamination dispersion in the range of tens to hundreds of kilometers, and it can track the evolution of diffusers through particle motion, making it the main business model for nuclear contamination dispersion prediction in various countries at present [10,23–25]. The Lagrangian model does not suffer from closure and numerical diffusion problems and is mathematically simpler than the Eulerian approach, but in regions far from the source of contamination, its accuracy decreases due to the reduction in the number of particles. In addition, because most of the meteorological forecasting models are based on Eulerian coordinates, diffusion models based on Lagrangian coordinates are difficult to couple synchronously with meteorological models, and they cannot make full use of the fine meteorological forecasting data [15,26,27].

The Eulerian model is suitable for simulating the spatial and temporal variations of the meteorological field, as well as complex physicochemical processes, especially the on-line coupled model of atmospheric chemistry that has been developed in recent years, and it can also take into account the feedback effect of pollutants on the meteorological field, and therefore, it is more effective in simulating the diffusion of large-scale and long-distance transport [26,28]. In nuclear pollution dispersion forecasting, Eulerian modeling is one of the important current development directions. Takemura et al. [29] and Christoudias et al. [30] simulated the wide-scale transport process of the Fukushima nuclear accident using the SPRINTARS and EMAC global atmospheric transport models, respectively. Ten Hoeve and Jacobson [31] developed a nuclide forecasting system for ^{131}I and ^{137}Cs based on the Eulerian-coordinate global–regional nested model GATOR-GCMOM and used it for the health hazard analysis of the Fukushima nuclear accident. Morino et al. [32] simulated the spatial and temporal variations in the deposition of ^{131}I and ^{137}Cs using the WRF-CMAQ atmospheric chemistry model. Kajino et al. [33] simulated ^{137}Cs from the Fukushima nuclear accident using the regional-scale NHM-Chem diffusion-transport model and found that ensemble-averaged meteorological fields were effective in reducing the simulation uncertainty. Bilgiç et al. [34] used a FLEXPART model to simulate the effects of vertical distribution patterns of Cs-137, released at eight different heights, on atmospheric diffusion and settlement during the Chernobyl nuclear power plant accident.

The Weather Research and Forecasting model Coupled to Chemistry (WRF-Chem) model [35] allows for the simultaneous computation of dynamic, radiative, and chemical processes to better simulate the parameterization interaction of meteorological and chemical fields. Hu et al. [36] added two nuclide variables, ^{131}I and ^{137}Cs, to the WRF-Chem model and investigated the effects of the schemes of microphysics, dry deposition, and wet deposition on the nuclide concentration and deposition for the Fukushima nuclear accident, and the results showed that the deposition of the radionuclide ^{137}Cs is very sensitive to microphysics schemes and wet deposition parameterization schemes. Fang et al. [37] optimized the atmospheric transport modeling of ^{137}Cs based on the WRF-Chem model by coupling 25 different ^{137}Cs in-cloud and under-cloud online wet scavenging scenarios with meteorological fields. Zhuang et al. [38] studied in-depth the detailed processes of 25 in-cloud and under-cloud wet scavenging modes using high-resolution (1 km $\times$ 1 km) meteorological inputs, based on the methods of Fang et al. [37], which showed that high-resolution meteorological inputs can more accurately reproduce local-scale ^{137}Cs concentrations.

Previous studies have mainly analyzed the horizontal transport of ^{137}Cs radionuclides, with fewer studies assessing vertical transport. Povinec et al. [39] used a Lagrangian model to simulate the dispersion of ^{137}Cs to the Americas and Europe as a result of the Fukushima nuclear accident. Fei et al. [40] simulated the dispersion of radioactive contaminants to the eastern Pacific Ocean and their arrival at the Americas after 5 days by means of the WRF and the Models-3/CMAQ coupled model. Long et al. [10] simulated the transport of ^{131}I and ^{137}Cs in the Fukushima nuclear accident using the FLEXPART model and found that radioactivity was transported via the Northern Hemisphere Rapids and the Northeastern Monsoon into the tropical Western Pacific Ocean and Southeast Asia.

In order to improve the accuracy of nuclear contamination model forecasting and to provide theoretical and technical support for regional nuclear contamination forecasting, warning, and emergency response, in this study, we constructed a scheme for radionuclide ^{137}Cs, based on the WRF-Chem model, considering the processes of advection, turbulent diffusion, dry deposition, and wet deposition. We designed two sets of comparative experiments, with and without deposition, for the period of high emissions from the Fukushima nuclear accident (11 to 17 March 2011) to simulate the spatial transport of ^{137}Cs and the ground deposition of the radionuclide ^{137}Cs, to analyze the characteristics of the spatial transport of the radionuclide ^{137}Cs in the horizontal and vertical directions, and to evaluate the effects of the wind field and precipitation on the spatial transport and ground deposition of the radionuclide ^{137}Cs.

2. Data and Methods

2.1. Data

Radionuclide monitoring concentration data were obtained from hour-by-hour radionuclide ^{137}Cs concentration data detected by SPM monitors in Bq·m^{-3} [3]. As shown in Figure 1, there are 32 stations in Japan, and the area with the largest pollution values of 02 UTC is in the inland area, with the highest concentration exceeding 300 Bq·m^{-3} at the highest station, and surpassing 22 UTC by late night. Thus, it is obvious that the maximum pollutant concentration on the east coast exceeds 150 Bq·m^{-3}; whereas, at this time, the pollutant concentration in the inland area is mostly less than 4 Bq·m^{-3}. In this study, we mainly utilized observation data from four stations with relatively high concentrations, namely Tokyo, Chiba, Maebashi, and Naraha. The radionuclide emission source uses the same radionuclide ^{137}Cs emission data obtained during the high emission period of the Fukushima nuclear accident (11 to 17 March 2011) used by Fang et al. [37] and Zhuang et al. [38].

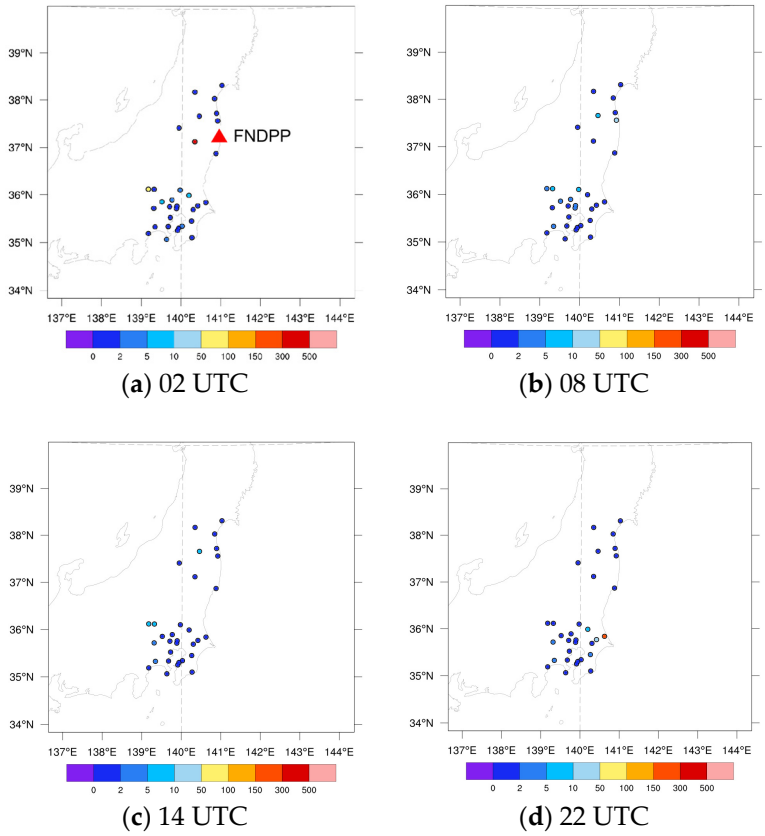

(**a**) 02 UTC (**b**) 08 UTC

(**c**) 14 UTC (**d**) 22 UTC

Figure 1. Radionuclide Cs-137 observation sites and their concentration distribution on 15 March 2011 (unit: Bq·m^{-3}).

Wind field data, including temperature, humidity, wind speed, and wind direction, were obtained from ground-based observatory site data released by the Japan Meteorological Agency (JMA), with a time resolution of 3 h (https://www.data.jma.go.jp/obd/stats/etrn/index.php, accessed on 11 May 2023). In this study, four observation stations, Tokyo and Chiba, in plain terrain, and Maebashi and Yamagata, in mountainous terrain, were selected for analysis.

Daily precipitation data were obtained from the Tropical Rainfall Measuring Mission (TRMM) rainfall figures, with a spatial resolution of 0.25° × 0.25° and a temporal resolution of 3 h. Daily cumulative precipitation was calculated by summing the results of the 3 h precipitation (https://disc.gsfc.nasa.gov/datasets/TRMM_3B42_Daily_7/summary, accessed on 11 May 2023).

Weather-driven data were obtained from the National Centers for Environmental Prediction (NCEP)/National Center for Atmospheric Research (NCAR) Global Final Analysis (FNL) (https://rda.ucar.edu/datasets/ds083.2, accessed on 11 May 2023), with a temporal resolution of 6 h and a spatial resolution of 1° × 1°. The main variables included temperature, humidity, wind direction, wind speed, air pressure at different atmospheric heights, and sea surface temperature.

2.2. WRF-Chem Model

The WRF-Chem model [35] can calculate dynamic, radiative, and chemical processes simultaneously to better simulate the interactions between meteorological and chemical fields, and it has been widely used in global and regional pollution studies [41]. In this study, version 3.9.1 of the WRF-Chem model was used, and the simulation period was from 11 March 2011 00:00 UTC (Universal Time Coordinated) to 17 March 2011 00:00 UTC. The simulation area is shown in Figure 2. Three nested grid areas were set up, with horizontal resolutions of 27 km, 9 km, and 3 km for areas d01, d02, and d03, respectively.

The d01 includes 181 × 150 grids, the d02 has 253 × 229 grids, and the innermost layer d03 is the main study area, with 211 × 250 grids, which encompasses the northeastern region of Japan, including the Kanto Plain region and the surrounding sea areas. The number of model layers in the vertical direction in regions d01, d02, and d03 was 30. The main physicochemical scheme of the model is shown in Table 1, which includes the Lin scheme [42], RRTM [43], and Dudhia [44] longwave and shortwave radiation schemes, respectively, as well as the Noah [45] land-surface parameterization scheme and the MYJ [46] planetary boundary layer scheme.

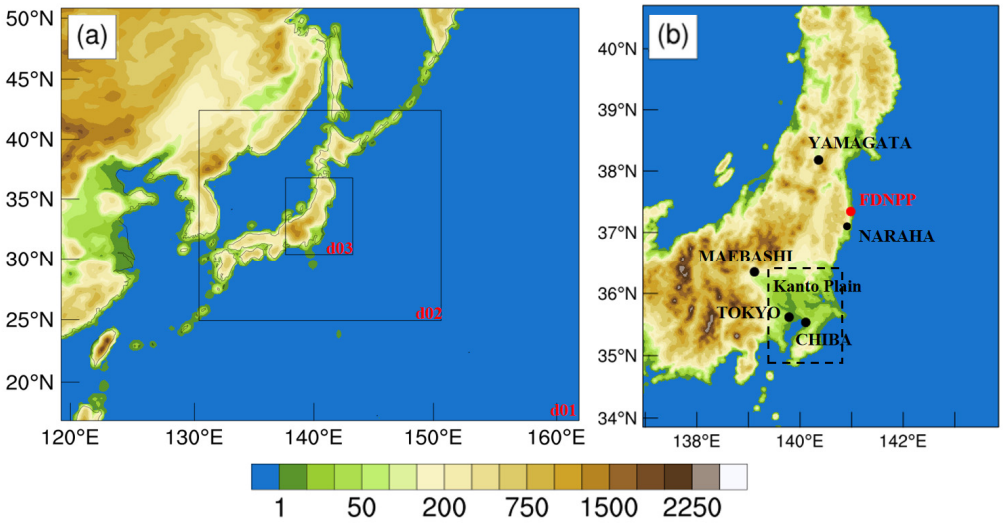

Figure 2. Maps of the WRF modeling domain; the color bars represent the terrain altitude. (**a**) domain 1, 2 and 3. (**b**) domain 3. The red dots on the right panel represent the location of the Fukushima nuclear power plant, the black dots represent the five ground-based observatories in Japan, and the black dashed box represents the Kanto Plain region in Japan.

Table 1. WRF-Chem model parameterized settings.

Physicochemical Scheme	Option
Microphysical scheme	Lin microphysics scheme [42]
Longwave radiation scheme	Rapid radiative transfer model [43]
Shortwave radiation scheme	Dudhia scheme [44]
Boundary layer scheme	Mellor–Yamada–Janjic scheme [46]
Land surface process	Noah land surface model [45]
Cumulus scheme	Grell 3-D scheme [47,48]

2.3. Parameterized Design of Radionuclide ^{137}Cs

Based on the WRF-Chem model and the theory of nuclear contamination dispersion, and referring to the parameterization scheme of Hu et al. [36], we designed a radionuclide parameterization scheme based on the description of Euler's advection–diffusion equations, including advection, turbulent diffusion, discharge, radioactive decay, and dry and wet deposition:

$$\frac{\partial A}{\partial t} = -div(uA) + div(\rho\kappa \cdot \nabla(\frac{A}{\rho})) - \wedge A - \lambda A + E \quad (1)$$

as shown in Table 2, where A is the air concentration of radionuclides (Bq·m^{-3}), which represents the radioactivity per unit volume of radionuclides. u is the wind vector, ∇ is the gradient of the air concentration of radionuclides, div is the dispersion of the air concentration of radionuclides, $\wedge$ is the wet scavenging rate of radionuclides (s^{-1}), λ represents the radioactive decay rate (s^{-1}), and E represents the point source of radionuclides. κ is the

turbulent diffusion coefficient. The radionuclide ^{137}Cs has a half-life of about 30 years, and the radioactive decay rate (7.33×10^{-10}) is low enough to neglect the decay process.

Table 2. List of symbols for the formulas used in this study.

Symbol	Meaning	Unit
A	the air concentration of radionuclides	Bq·m^{-3}
∇	the gradient of the air concentration of radionuclides	
div	the dispersion of the air concentration of radionuclides	
$\wedge$	the wet scavenging rate of radionuclides	s^{-1}
λ	the radioactive decay rate	s^{-1}
E	the point source of radionuclides	
κ	the turbulent diffusion coefficient	
W	the air concentration of ^{137}Cs	μg·kg^{-1}
M	the molar mass of ^{137}Cs	g·mol^{-1}
N_A	Avogadro's constant	mol^{-1}
ρ_{air}	the density of air	kg·m^{-3}
D_{gr}	the surface dry deposition	Bq·m^{-2}
t	the deposition duration	
v_{dep}	the dry deposition rate	m·s^{-1}
W_{gr}	the surface wet deposition	Bq·m^{-2}
h	the height of the area	
p_0	the precipitation rate	mm·h^{-1}
a	constant	8×10^{-5}
b	constant	0.8

In addition, in the WRF-Chem model, the default unit of aerosol is μg·kg^{-1}, while the unit of radionuclide concentration is Bq·m^{-3}: the unit conversion equation between the two is:

$$\frac{W}{M} = \frac{A}{\lambda N_A \rho_{air}} \times 10^6 \quad (2)$$

as shown in Table 2, where W is the air concentration of ^{137}Cs in μg·kg^{-1}; A is the air concentration of ^{137}Cs in Bq·m^{-3}; A (g·mol^{-1}) is the molar mass of ^{137}Cs; λ (s^{-1}) is the radioactive decay rate of ^{137}Cs; $N_A 1$ (mol^{-1}) is Avogadro's constant, and ρ_{air} (kg·m^{-3}) is the density of air.

2.3.1. Dry Deposition

Dry deposition is an important physical process in the modeling of pollutant dispersion in the atmosphere, which is assumed to be independent of factors such as clouds and precipitation and can be calculated using Equation (3):

$$D_{gr}(t) = \int_{t_0}^{t} -v_{dep} A e^{-\lambda t} dt \quad (3)$$

as shown in Table 2, where D_{gr} is the surface dry deposition in Bq·m^{-2}, t is the deposition duration, and v_{dep} is the dry deposition rate.

2.3.2. Wet Deposition

Similar to the calculation of surface deposition for dry deposition, the wet removal rate must be considered in the calculation of surface deposition for wet deposition, and it can be calculated using Equation (4):

$$W_{gr}(t) = \int_{t_0}^{t} \int_{0}^{h} \wedge(z) A(z) e^{-\lambda t} dz dt \quad (4)$$

as shown in Table 2, where W_{gr} is the surface wet deposition in Bq·m^{-2}, and h is the height of the area. The wet deposition rate can be calculated from the precipitation rate:

$$\wedge = ap_0{}^b \tag{5}$$

as shown in Table 2, where p_0 is the precipitation rate (mm·h^{-1}), and a and b are constants. For ^{137}Cs, $a = 8 \times 10^{-5}$ and $b = 0.8$ [49].

2.4. Simulation of Experimental Design

In this study, two sets of sensitivity simulation experiments on nuclide forecasting were designed to assess the effect of the presence or absence of dry and wet deposition on the spatial transport and surface deposition of ^{137}Cs in the atmosphere (Table 3), where the control experiment was without dry and wet deposition, and EX_Dep was a sensitivity experiment, with dry and wet deposition. The same WRF-Chem parameterization scheme and emission sources were used in both sets of tests.

Table 3. Sensitivity simulation test design for radionuclide prediction.

Experiment Name	Experiment Design
Control	No dry and wet deposition
EX_Dep	Dry and wet deposition

2.5. Evaluation of Simulation Results Testing

In this study, the correlation coefficient (CORR), mean bias (BIAS), root mean square error (RMSE), percent bias (PBIAS), percent root mean square error (PRMSE), and specific activity of air (FAC5/FAC10) were used to test and evaluate the simulation results of the WRF-Chem model, the specific formulas of which can be found in Equations (6)–(11):

$$CORR = \frac{cov(D_s, D_o)}{\sigma_s \sigma_o} \tag{6}$$

$$BIAS = \frac{\sum_i^N (D_{si} - D_{oi})}{N} \tag{7}$$

$$RMSE = \sqrt{\frac{\sum_i^N (D_{si} - D_{oi})^2}{N}} \tag{8}$$

$$PBAIS = \frac{\frac{1}{N}\sum_i^N (D_{si} - D_{oi})}{\frac{1}{N}\sum_i^N D_{oi}} \times 100\% \tag{9}$$

$$PRMSE = \frac{\sqrt{\frac{1}{N}\sum_i^N (D_{si} - D_{oi})^2}}{\frac{1}{N}\sum_i^N D_{oi}} \times 100\% \tag{10}$$

$$FAC5/10 = \frac{D_{si}}{D_{oi}} \tag{11}$$

where N is the number of samples, D_o is the set of observations, D_s is the set of simulations, D_{oi} is the observed value, D_{si} is the simulated value, and i represents the first simulated data in the set of observations or simulations. The air-specific activities FAC5 and FAC10 represent the ratio of simulated and observed forecasts in the range of 0.2~5 and 0.1~10, respectively, and the larger the value, the smaller the difference between the simulated value and the observed value and the higher the accuracy of the simulation.

3. Results and Discussion

3.1. Meteorological Field Simulation Analysis

Figure 3 and Table 4 show the time series plots of the observed and simulated wind speeds and directions, and the results of the BIAS and RMSE tests of wind speed and direction for the stations in Tokyo, Chiba, Maebashi, and Yamagata from 11 to 17 March 2011. It can be seen that the model can simulate the wind speed and direction change characteristics more accurately, especially at the Chiba site, where the simulation results of the model wind speed are the closest to the observed results. The BIAS of the wind speed at the Tokyo, Chiba, Maebashi, and Yamagata sites was 0.55 $m \cdot s^{-1}$, 0.41 $m \cdot s^{-1}$, 0.58 $m \cdot s^{-1}$, and 1.37 $m \cdot s^{-1}$, whereas the RMSE was 1.57 $m \cdot s^{-1}$, 1.54 $m \cdot s^{-1}$, 1.79 $m \cdot s^{-1}$, and 1.90 $m \cdot s^{-1}$, respectively. The BIAS of the wind direction at the Tokyo, Chiba, Maebashi, and Yamagata sites was 6.27°, 7.08°, 9.10°, and −7.17°, whereas the RMSE was 62.86°, 44.84°, 74.07°, and 72.60°, respectively. At the Maebashi and Yamagata stations, the differences between the simulation results for wind speed and direction and the observed data are relatively large, which may be due to the fact that these stations are in the mountainous region, and the actual wind speeds are usually affected by the friction of the terrain, whereas the modeled terrain is relatively smooth; thus, the modeled wind speeds are slightly higher than the actual speed.

Table 4. BIAS and RMSE test results for wind speed and direction from 11–17 March 2011.

		Tokyo	Chiba	Maebashi	Yamagata
BIAS	Wind speed	0.55	0.41	0.58	1.37
	Wind direction	6.27	7.08	9.1	−7.17
RMSE	Wind speed	1.57	1.54	1.79	1.90
	Wind direction	62.86	44.84	74.27	72.60

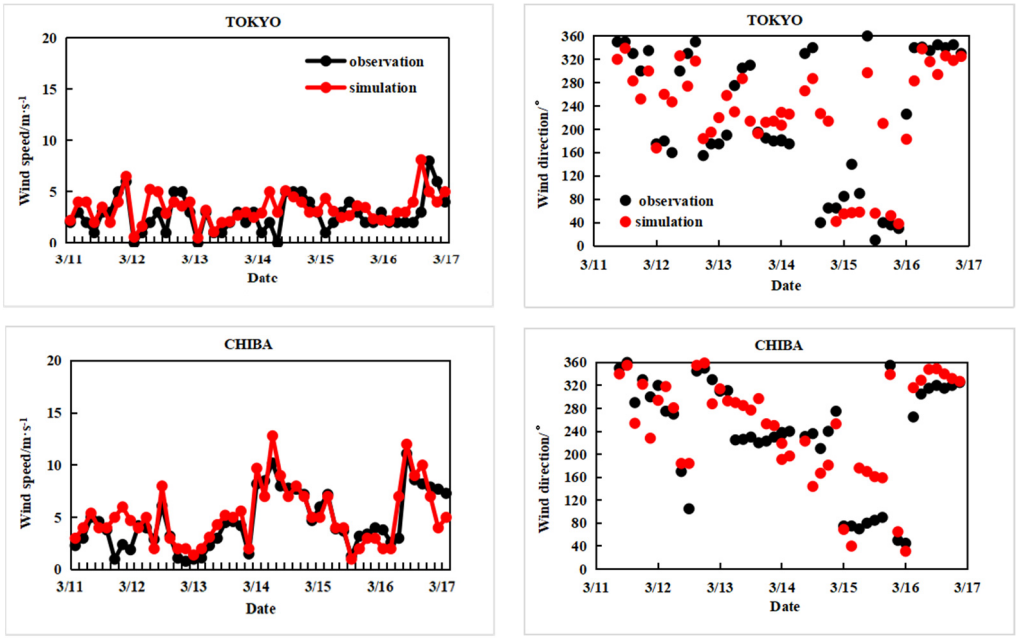

Figure 3. *Cont.*

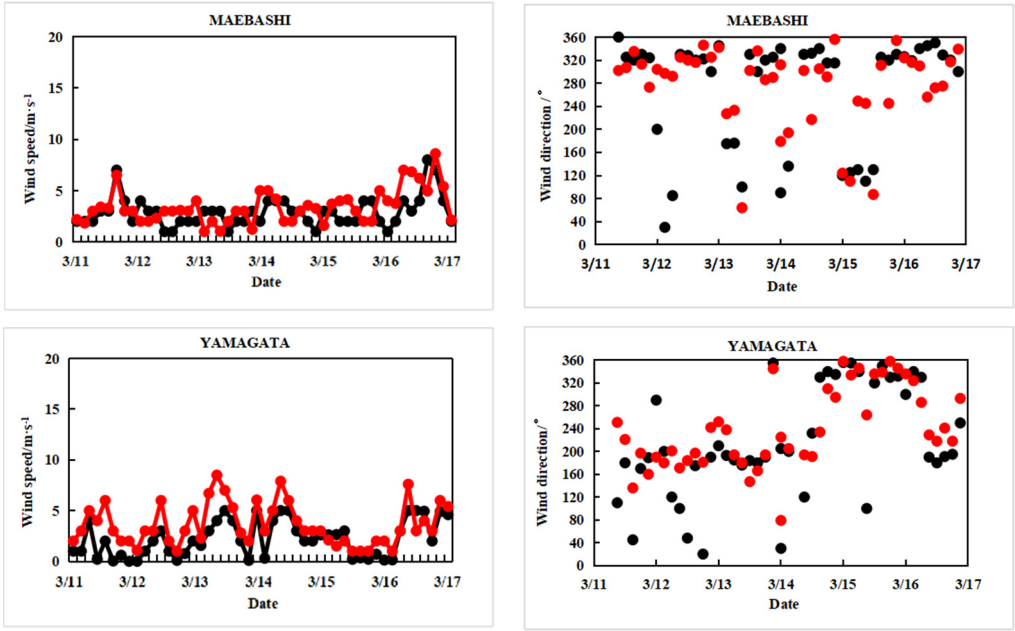

Figure 3. Time series of observed and simulated surface wind speed and direction at four weather stations in Japan from 11–17 March 2011.

Figure 4 shows the daily precipitation distribution on 15 March 2011 from TRMM satellite observations and model simulations. As can be seen in the figure, the precipitation on 15 March is mainly concentrated in the northeastern region of Japan and the eastern ocean region, and the maximum precipitation of more than 40 mm·day^{-1} is located in the northeastern region of Japan. The model's simulated precipitation distribution for 15 March was basically the same as that observed rate; however, it slightly underestimated the precipitation in the northeastern region of Japan, whereas the simulated precipitation in the eastern oceanic region was slightly overestimated.

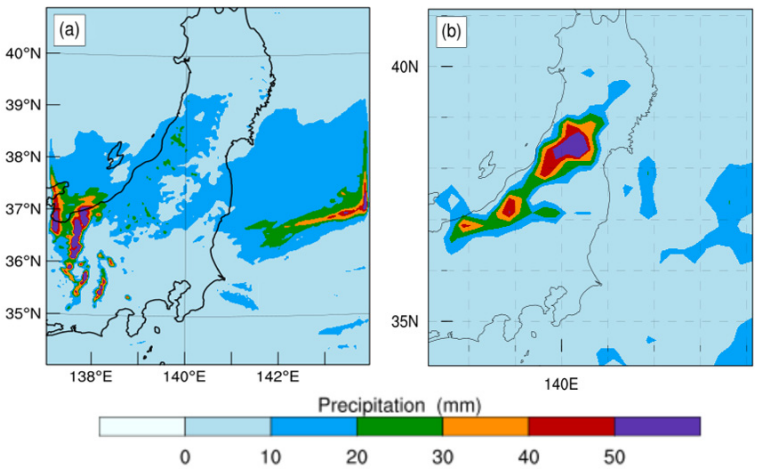

Figure 4. Observed and simulated daily precipitation on 15 March 2011. (**a**) Observed daily cumulative precipitation; (**b**) simulated daily cumulative precipitation.

Figure 5 shows the time-series plots of precipitation from 11–17 March 2011 at the Yamagata and Maebashi stations. We only analyzed the time-series plots of precipitation at the Yamagata and Maebashi stations because there was no precipitation during the study period in either the observations or simulations at the Tokyo and Chiba stations. As can be seen from the figure, the simulated and observed precipitation at the Yamagata and Maebashi stations are in good agreement. The observed and simulated precipitation at

the Yamagata station occurred on 11, 12, 15, and 16 March, the observed precipitation at the Maebashi station occurred on 16 March, and the simulated precipitation mainly occurred on 15 and 16 March. Both models overestimated the maximum precipitation at the Yamagata and Maebashi stations during the study period.

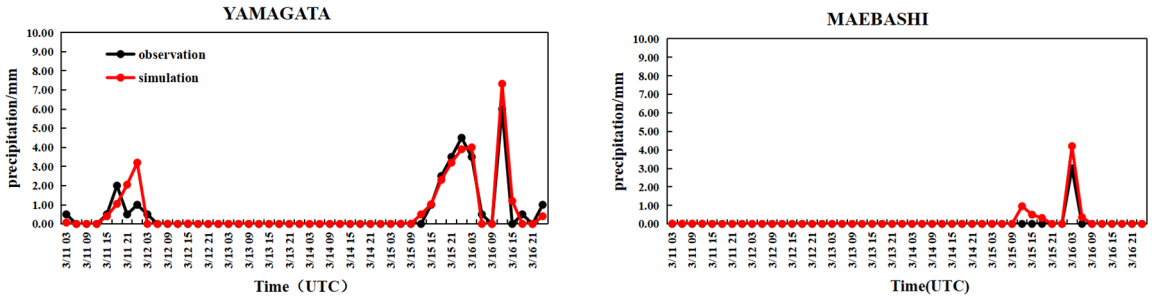

Figure 5. Time series of observed and simulated precipitation at the Yamagata and Maebashi weather stations from 11 to 17 March 2011.

3.2. Analysis of the Spatial Transport of Radionuclide ^{137}Cs

Figure 6 shows the simulated near-surface concentrations of ^{137}Cs from the Control test and the EX_Dep test on 15 March 2011, which shows that the ^{137}Cs emitted from Fukushima at 06:00 UTC on 15 March were first dispersed inland in the southwestern part of Japan, driven by northeasterly winds (Figure 6a,e). At 12:00 UTC, northeasterly winds increased offshore east of Fukushima, while wind speeds were lower west and south of Fukushima, thus creating a convergence of the wind field along the coast, and the ^{137}Cs concentration was distributed in a band along the coastline south of Fukushima (Figure 6b,f). At 18:00 UTC, ^{137}Cs spread further southward, but owing to the southeasterly winds in the offshore area south of Chiba, it formed a convergence zone with northerly winds to the north, which resulted in the formation of an east–west zone of high values over Chiba and its eastern oceanic surface (Figure 6c,g). At 23:00 UTC, the entire contaminated area was pushed east–south due to the strengthening of the north wind and its gradual shift to the northwest (Figure 6d,h). Since dry and wet deposition were not considered in the Control test, the simulated ^{137}Cs concentration was higher, and the ^{137}Cs concentration near Fukushima at 06:00 UTC was more than 500 Bq·m^{-3}. The EX_Dep test simulated a more similar distribution of ^{137}Cs compared with that of the Control test, but the concentration was much lower than that of the Control test and closer to the observed values. In the EX_DEP test, ^{137}Cs concentration in the Fukushima area at 06:00 UTC decreased to about 300 Bq·m^{-3} compared with the results of the Control test, with a reduction of about 286 Bq·m^{-3} (Figure 6a,e).

Figure 7 shows the height–time profile of the vertical wind field over the Fukushima nuclear power plant from 14 to 16 March 2011, the time series of hourly precipitation, and the height–time profile of ^{137}Cs concentration. As shown in Figure 7a, the lower atmosphere was dominated by an upward motion from 14 to 16 March, with a downward motion mainly from 05:00 to 10:00 UTC on 14 March and from 10:00 to 20:00 UTC on 16 March, when the upward flow promoted the upward vertical diffusion of ^{137}Cs, while the downward flow inhibited the vertical diffusion of ^{137}Cs. The diffusion heights of ^{137}Cs in the vertical direction from 05:00~10:00 UTC on 14 March and from 10:00~20:00 UTC on 16 March (Figure 7c,d) were relatively low. However, the diffusion height of ^{137}Cs in the vertical direction was relatively high from 06:00 to 18:00 UTC on 15 March, and the highest diffusion of ^{137}Cs up to an altitude of 6 km in the Control test was related to stronger vertical upward motion at the corresponding moment, as shown in Figure 7a. The diffusion heights of ^{137}Cs in the EX_Dep test were generally lower than those in the Control test due to both dry and wet deposition, especially on 14 March between 00:00~06:00 UTC, 15 March between 08:00~12:00 UTC, and 16 March between 00:00~10:00 UTC. The vertical diffusion heights were significantly lower than those of the Control test, which is related

to the wet deposition caused by precipitation at the corresponding moments, as shown Figure 7b.

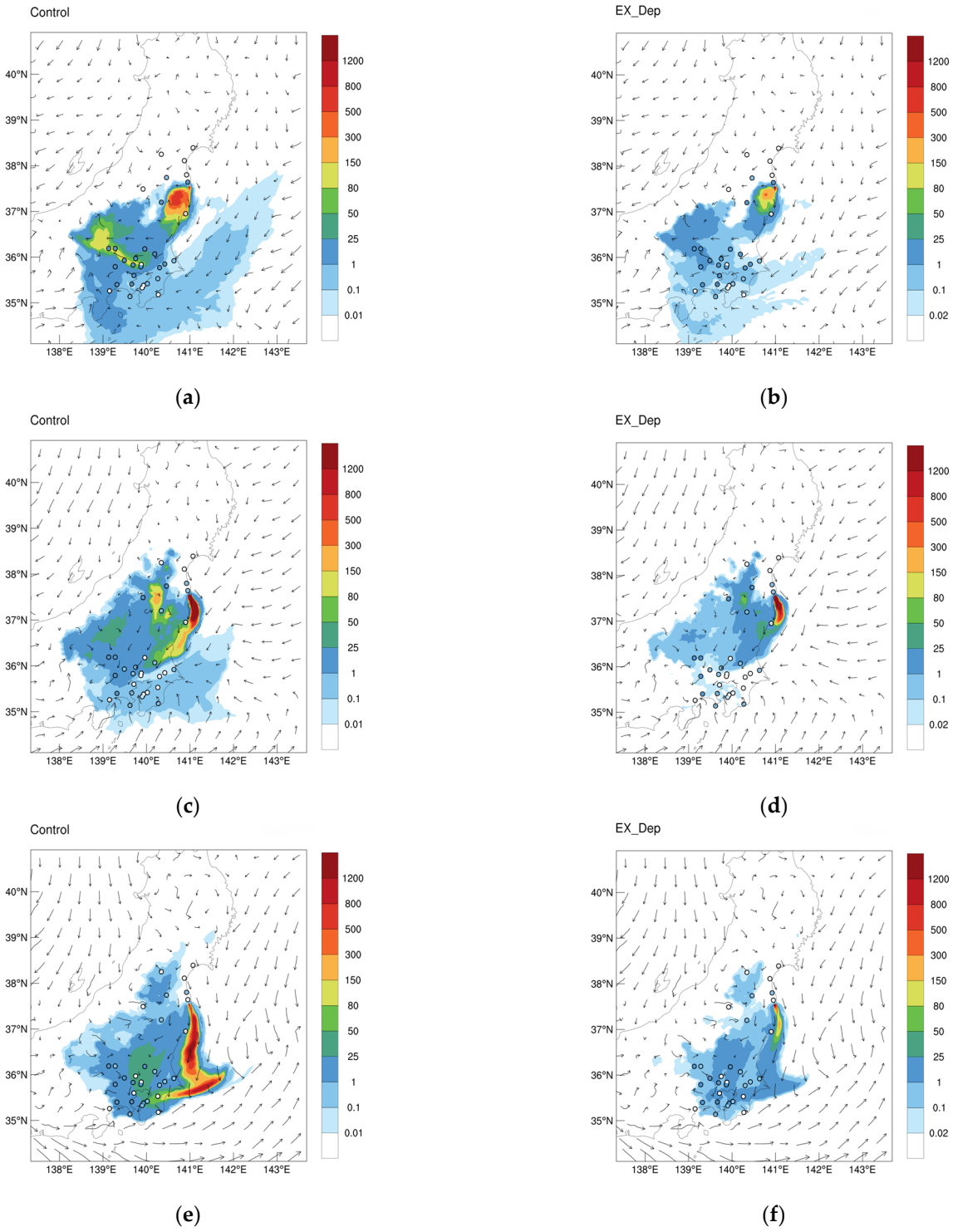

Figure 6. *Cont.*

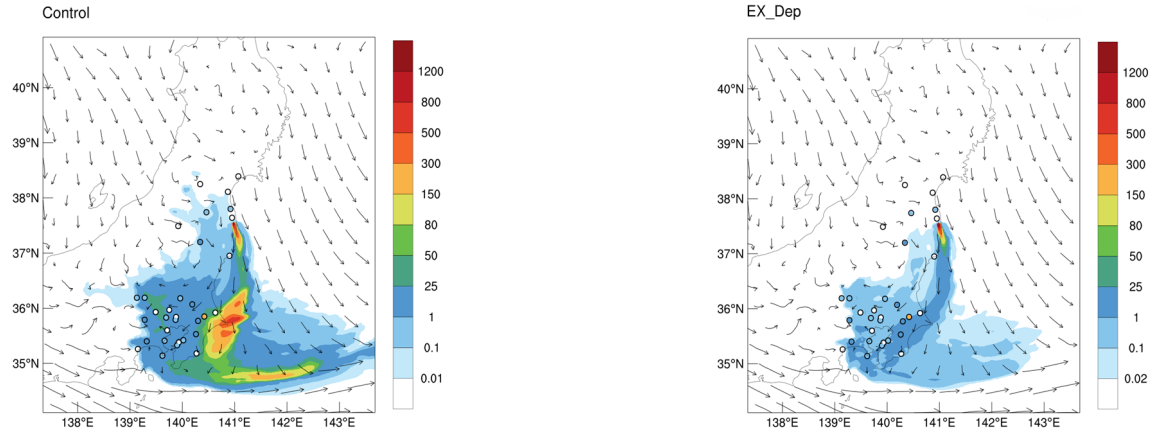

(**g**) (**h**)

Figure 6. The near-surface concentration of ^{137}Cs simulated in the Control experiment (top) and the EX_Dep experiment (bottom) on 15 March 2011. (**a**,**b**) 06:00; (**c**,**d**) 12:00; (**e**,**f**) 18:00; (**g**,**h**) 23:00. The scatter indicates the observed value at that moment in time. Concentrations are in Bq·m^{-3}.

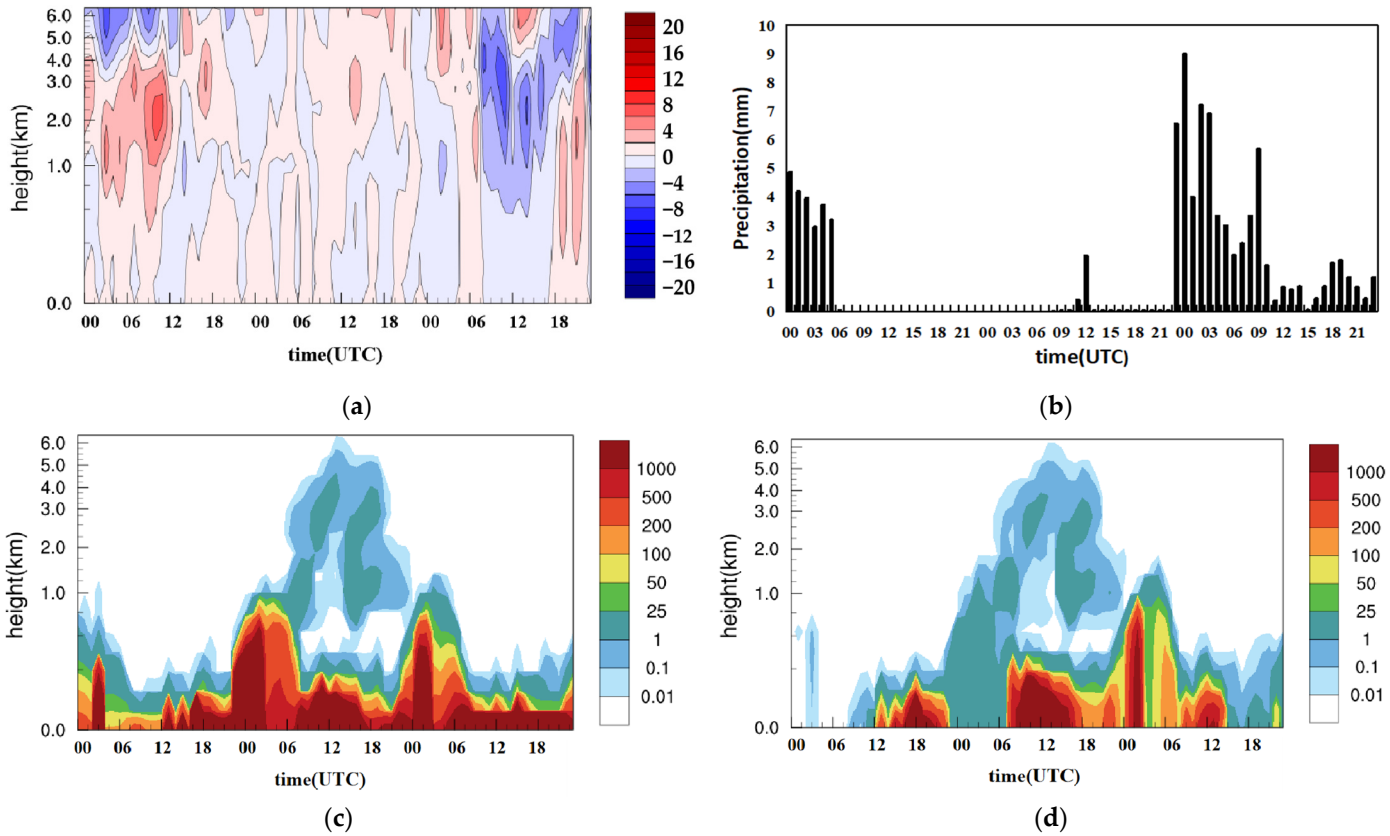

(**a**) (**b**)

(**c**) (**d**)

Figure 7. Height–time profile of vertical wind field over Fukushima Nuclear Power Plant, time series of hourly precipitation and height–time profile of ^{137}Cs concentration from 14 to 16 March 2011. (**a**) Vertical wind field height–time profiles, (**b**) hourly precipitation time series plots, (**c**) height–time profiles of ^{137}Cs concentrations in the Control test, and (**d**) height–time profiles of ^{137}Cs concentrations in the EX_Dep test. Wind speed, precipitation, and ^{137}Cs concentration are in dm·s^{-1}, mm, and Bq·m^{-3}, respectively.

3.3. Radionuclide ^{137}Cs Ground Deposition Analysis

Figure 8 shows the spatial distribution of the dry and wet deposition of ^{137}Cs on 15 March 2011. It can be seen that the dry deposition is mainly located in the Fukushima and Kanto areas and their eastern and southern oceanic regions (Figure 8a) due to the wind field. The wet deposition (Figure 8b) is mainly affected by precipitation, which was observed in Fukushima and its eastern oceanic regions (Figure 4a) on 15 March and was mainly concentrated in the vicinity of the Fukushima and Kanto Plain areas and their eastern oceanic regions. The range of wet deposition was significantly greater than that of dry deposition, which was much higher than wet deposition, with the maximum dry deposition of 5004.5 kBq·m^{-2}, and the maximum wet deposition of 725.3 kBq·m^{-2}. As a result of dry and wet deposition, the concentration of radionuclide ^{137}Cs in the Kanto area and its eastern ocean region in the EX_DEP test was substantially reduced compared with that of the Control test, and the ^{137}Cs concentration was closer to the actual observed concentration (Figure 6).

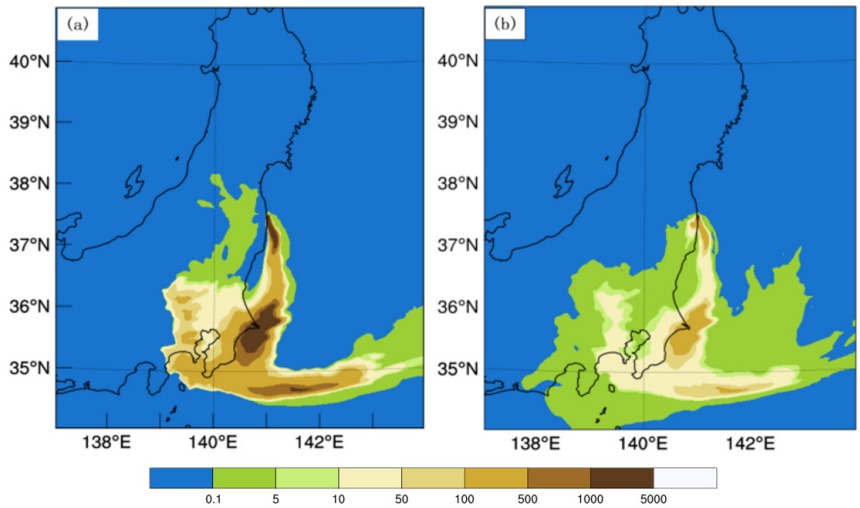

Figure 8. The spatial distribution of dry and wet deposition of ^{137}Cs on 15 March 2011. (**a**) dry deposition. (**b**) wet deposition.

3.4. Analysis of Radionuclide ^{137}Cs Site Concentrations

Figure 9 shows the time series plots of the observed and modeled concentrations of ^{137}Cs on 15 March 2011 at four different stations sites for the Control and EX_Dep tests. As can be seen in the figure, the concentration of ^{137}Cs observed at the Tokyo site was relatively low, with an average concentration of less than 10 Bq·m^{-3} over the study period, and the peak concentrations of ^{137}Cs observed at the Chiba, Maebashi, and Naraha sites were 30 Bq·m^{-3}, 59 Bq·m^{-3}, and 93 Bq·m^{-3}, respectively. Due to the dry and wet deposition effects, the ^{137}Cs concentrations at the Tokyo, Chiba, Maebashi, and Naraha stations in the EX_Dep test were lower than those in the Control test and were closer to the observed values. The delay of the peak at the Maebashi station in the Control test was corrected, and the overestimation of the peak concentration was improved in the EX_Dep test.

Table 5 shows the results of ^{137}Cs concentration on 15 March 2011 for the Control and EX_Dep tests for each station. As can be seen in the table, the single-site test results of the EX_Dep test were all better than those of the Control test, with the Tokyo, Chiba, Maebashi, and Naraha sites experiencing improvements in CORR of 8%, 4%, 5%, and 4%, respectively. For the Tokyo, Chiba, Maebashi, and Naraha stations, improvements in FAC10 of 17%, 16%, 6%, and 6%, decreases in PBIAS of 61%, 69%, 46%, and 51%, and decreases in PRMSE of 46%, 25%, 38%, and 48%, respectively, were observed.

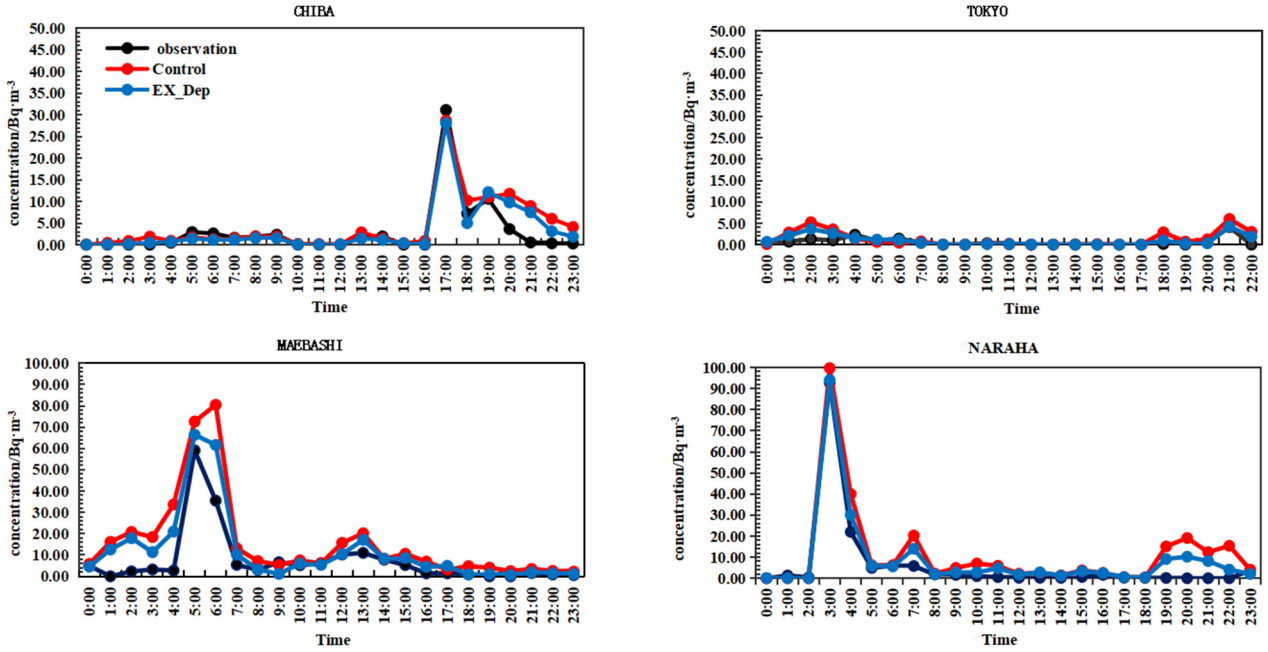

Figure 9. Time series of observed and simulated concentrations of ^{137}Cs at four sites for the Control and EX_Dep experiment on 15 March 2011.

Table 5. Single station test results for ^{137}Cs concentration in Control and EX_Dep experiments on 15 March 2011.

Station	Experiment Name	CORR	PBIAS	PRMSE	FAC5	FAC10
Tokyo	Control	0.75	79%	162%	0.54	0.54
	EX_Dep	0.81	31%	89%	0.58	0.63
Chiba	Control	0.81	42%	102%	0.50	0.50
	EX_Dep	0.84	13%	77%	0.52	0.58
Maebashi	Control	0.78	112%	184%	0.75	0.83
	EX_Dep	0.82	61%	114%	0.75	0.88
Naraha	Control	0.85	87%	137%	0.46	0.63
	EX_Dep	0.88	43%	71%	0.5	0.67

4. Conclusions

By analyzing in detail the diffusion and deposition of ^{137}Cs radionuclides, especially vertical diffusion, as well as the effects of the wind field and precipitation on diffusion and deposition, this study provides an important basis for a more comprehensive understanding of the behavior of radionuclides after nuclear accidents, offering theoretical and technical support for regional nuclear pollution prediction, early warning, and emergency response. In this paper, a parameterization scheme for radionuclide ^{137}Cs was constructed based on the WRF-Chem model, and two sets of comparison experiments, with and without deposition, were designed to simulate the spatial transport of ^{137}Cs and the ground deposition process after the Fukushima nuclear accident from 11 to 17 March 2011. This was conducted to analyze the characteristics of the spatial transport of ^{137}Cs in the horizontal and vertical directions and to evaluate the effects of the wind field and precipitation on the spatial transport of ^{137}Cs and the ground deposition. The main conclusions are as follows:

Wind field and precipitation are important factors affecting the horizontal and vertical dispersion of ^{137}Cs in the atmosphere. On 15 March, ^{137}Cs was generally dispersed towards the Kanto Plain region of Japan under the influence of northeasterly winds, and the concentrations were mainly concentrated in the Fukushima and Kanto Plain regions. Compared with the no-deposition test, the concentration of ^{137}Cs in the Fukushima area in the deposition test decreased by about 286 Bq·m^{-3}; ^{137}Cs in the no-deposition test could be

dispersed upward up to an altitude of 6 km under the effect of updraft, while those in the deposition test could only be dispersed up to an altitude of 4 km.

Dry and wet depositions are important processes for removing radionuclides from the atmosphere and are significantly influenced by wind fields and precipitation. On 15 March, the dry deposition and wet deposition area of ^{137}Cs was mainly located in Fukushima, the Kanto Plain, and the eastern ocean region, under the influence of the wind field and precipitation, with the maximum dry deposition of 5004.5 kBq·m^{-2} and the maximum wet deposition of 725.3 kBq·m^{-2}.

The single-station test results of the deposition test were better than those of the no-deposition test, with correlation coefficients at the Tokyo, Chiba, Maebashi, and Naraha sites improving by 8%, 4%, 5%, and 4%, respectively, the air specific activity improving by 17%, 16%, 6%, and 6%, the percentage deviations decreasing by 61%, 69%, 46%, and 51%, and the percentage root mean square errors decreasing by 46%, 25%, 38%, and 48%, respectively.

Author Contributions: Conceptualization, Z.Z.; software, Q.L., Y.H., Y.W. and S.Z.; formal analysis, Q.L.; writing—original draft preparation, Q.L.; writing—review and editing, Z.Z. and X.M.; supervision, S.F. and L.W. All authors have read and agreed to the published version of the manuscript.

Funding: This research has been jointly supported by the National Natural Science Foundation of China (Grant 42375032).

Institutional Review Board Statement: Not applicable.

Informed Consent Statement: Not applicable.

Data Availability Statement: The data presented in this study are available on request from the corresponding author. The data are not publicly available due to restrictions privacy.

Conflicts of Interest: The authors declare no conflict of interest.

References

1. Fujii, Y.; Satake, K.; Sakai, S.; Shinohara, M.; Kanazawa, T. Tsunami source of the 2011 off the pacific coast of tohoku earthquake. *Earth Planets Space* **2011**, *63*, 815–820. [CrossRef]
2. Stohl, A.; Seibert, P.; Wotawa, G.; Arnold, D.; Burkhart, J.F.; Eckhardt, S.; Tapia, C.; Vargas, A.; Yasunari, T.J. Xenon-133 and caesium-137 releases into the atmosphere from the Fukushima Dai-ichi nuclear power plant: Determination of the source term, atmospheric dispersion, and deposition. *Atmos. Chem. Phys.* **2012**, *12*, 2313–2343. [CrossRef]
3. Tsuruta, H.; Oura, Y.; Ebihara, M.; Ohara, T.; Nakajima, T. First retrieval of hourly atmospheric radionuclides just after the Fukushima accident by analyzing filter-tapes of operational air pollution monitoring stations. *Sci. Rep.* **2014**, *4*, 6717. [CrossRef] [PubMed]
4. Diaz Leon, J.; Jaffe, D.A.; Kaspar, J.; Knecht, A.; Miller, M.L.; Robertson, R.G.H.; Schubert, A.G. Arrival time and magnitude of airborne fission products from the Fukushima, Japan, reactor incident as measured in Seattle, WA, USA. *J. Environ. Radioact.* **2011**, *102*, 1032–1038. [CrossRef] [PubMed]
5. MacMullin, S.; Giovanetti, G.K.; Green, M.P.; Henning, R.; Holmes, R.; Vorren, K.; Wilkerson, J.F. Measurement of airborne fission products in Chapel Hill, NC, USA from the Fukushima Dai-ichi reactor accident. *J. Environ. Radioact.* **2012**, *112*, 165–170. [CrossRef] [PubMed]
6. Sinclair, L.E.; Seywerd, H.C.J.; Fortin, R.; Carson, J.M.; Saull, P.R.B.; Coyle, M.J.; Van Brabant, A.; Buckle, J.L.; Desjardins, S.M.; Hall, R.M. Aerial measurement of radioxenon concentration off the west coast of Vancouver Island following the Fukushima reactor accident. *J. Environ. Radioact.* **2011**, *102*, 1018–1023. [CrossRef] [PubMed]
7. Simgen, H.; Arnold, F.; Aufmhoff, H.; Baumann, R.; Kaether, F.; Lindemann, S.; Rauch, L.; Schlager, H.; Schlosser, C.; Schumann, U. Detection of (133)Xe from the Fukushima nuclear power plant in the upper troposphere above Germany. *J. Environ. Radioact.* **2014**, *132*, 94–99. [CrossRef]
8. Bolsunovsky, A.; Dementyev, D. Evidence of the radioactive fallout in the center of Asia (Russia) following the Fukushima Nuclear Accident. *J. Environ. Radioact.* **2011**, *102*, 1062–1064. [CrossRef] [PubMed]
9. Long, N.Q.; Truong, Y.; Hien, P.D.; Binh, N.T.; Sieu, L.N.; Giap, T.V.; Phan, N.T. Atmospheric radionuclides from the Fukushima Dai-ichi nuclear reactor accident observed in Vietnam. *J. Environ. Radioact.* **2012**, *111*, 53–58. [CrossRef]
10. Long, P.K.; Hien, P.D.; Quang, N.H. Atmospheric transport of 131I and 137Cs from Fukushima by the East Asian northeast monsoon. *J. Environ. Radioact.* **2019**, *197*, 74–80. [CrossRef]
11. Kim, C.K.; Byun, J.I.; Chae, J.S.; Choi, H.Y.; Choi, S.W.; Kim, D.; Kim, Y.J.; Lee, D.M.; Park, W.J.; Yim, S.; et al. Radiological impact in Korea following the Fukushima nuclear accident. *J. Environ. Radioact.* **2012**, *111*, 70–82. [CrossRef] [PubMed]

12. Zhang, W.-J.; Xu, Y.-S.; Xu, J.; He, Y.-J.; Zhao, X.-Y.; Meng, F.; Bai, Z.-P. Impact of Japan's Nuclear Leakage on the Typical Areas of Northern China. *Res. Environ. Sci.* **2013**, *26*, 274–280.
13. Onda, Y.; Taniguchi, K.; Yoshimura, K.; Kato, H.; Takahashi, J.; Wakiyama, Y.; Coppin, F.; Smith, H.G. Radionuclides from the Fukushima Daiichi Nuclear Power Plant in terrestrial systems. *Nat. Rev. Earth Env.* **2020**, *1*, 644–660. [CrossRef]
14. Wai, K.M.; Yu, P.K. Trans-oceanic transport of 137Cs from the Fukushima nuclear accident and impact of hypothetical Fukushima-like events of future nuclear plants in Southern China. *Sci. Total Environ.* **2015**, *508*, 128–135. [CrossRef] [PubMed]
15. Chi, Y.Y.; Zhuang, H.Y. A Review of Applied Research on Air Pollutant Dispersion Modelling. *Environ. Pollut. Prev.* **2007**, *29*, 6. [CrossRef]
16. Ge, B.Z.; Lu, Q.Q.; Chen, X.S.; Wang, Z.F. A review of the numerical simulations of the atmospheric dispersion of radionuclides. *Acta Sci. Circumstantiae* **2021**, *41*, 1599–1609. [CrossRef]
17. Hultquist, C.; Cervone, G. Comparison of simulated radioactive atmospheric releases to citizen science observations for the Fukushima nuclear accident. *Atmos. Environ.* **2018**, *198*, 478–488. [CrossRef]
18. Mészáros, R.; Leelőssy, Á.; Kovács, T.; Lagzi, I. Predictability of the dispersion of Fukushima-derived radionuclides and their homogenization in the atmosphere. *Sci. Rep.* **2016**, *6*, 19915. [CrossRef] [PubMed]
19. Chanin, D.I.; Sprung, J.L.; Ritchie, L.T.; Jow, H.N. *MELCOR Accident Consequence Code System (MACCS)*; Division of Systems Research, Nuclear Regulatory Commission: Washington, DC, USA; Sandia National Laboratories: Albuquerque, NM, USA, 1990.
20. Fang, S.; Li, H.; Fang, D. Application of ARCON96 in the evaluation of the habitability of the main control room of nuclear power plant and its comparison with the combined wake model. *Radiat. Prot.* **2012**, *32*, 7.
21. Zhuo, J.; Huang, L.X.; Niu, S.L.; Xie, H.G.; Kuang, F.H. A random walk model to simulate the atmospheric dispersion of radionuclide. *IOP Conf. Ser. Earth Environ. Sci.* **2018**, *108*, 042017. [CrossRef]
22. Li, H.; Deng, J.-Y.; Wang, X.-H.; Zhang, L.-X. Diffusion of radionuclide clouds in the atmosphere using Gaussian modelling. *Radiat. Prot.* **2004**, *24*, 92–99.
23. Stein, A.F.; Draxler, R.R.; Rolph, G.D.; Stunder, B.J.B.; Cohen, M.D.; Ngan, F. NOAA's HYSPLIT Atmospheric Transport and Dispersion Modeling System. *Bull. Am. Meteorol. Soc.* **2015**, *96*, 2059–2077. [CrossRef]
24. Stohl, A.; Forster, C.; Frank, A.; Seibert, P.; Wotawa, G. Technical note: The Lagrangian particle dispersion model FLEXPART version 6.2. *Atmos. Chem. Phys.* **2005**, *5*, 2461–2474. [CrossRef]
25. Yao, R.T.; Xu, X.J.; Hao, H.W.; Yao, Q.S. Modelling of long-range transport of airborne radioactive contaminants released from nuclear risk sites in the Far East region. *Radiat. Prot.* **2005**, *25*, 13. [CrossRef]
26. Leelőssy, Á.; Lagzi, I.; Kovács, A.; Mészáros, R. A review of numerical models to predict the atmospheric dispersion of radionuclides. *J. Environ. Radioact.* **2018**, *182*, 20–33. [CrossRef] [PubMed]
27. Tsang, Y.; Vallis, G.K. A stochastic Lagrangian basis for a probabilistic parameterization of moisture condensation in Eulerian models. *J. Atmos. Sci.* **2018**, *75*, 3925–3941. [CrossRef]
28. Kajino, M.; Sekiyama, T.T.; Mathieu, A.; Korsakissok, I.; Périllat, R.; Quélo, D.; Quérel, A.; Saunier, O.; Adachi, K.; Girard, S.; et al. Lessons learned from atmospheric modeling studies after the Fukushima nuclear accident: Ensemble simulations, data assimilation, elemental process modeling, and inverse modeling. *Geochem. J.* **2018**, *52*, 85–101. [CrossRef]
29. Takemura, T.; Nakamura, H.; Takigawa, M.; Kondo, H.; Satomura, T.; Miyasaka, T.; Nakajima, T. A Numerical Simulation of Global Transport of Atmospheric Particles Emitted from the Fukushima Daiichi Nuclear Power Plant. *Sci. Online Lett. Atmos. SOLA* **2011**, *7*, 101–104. [CrossRef]
30. Christoudias, T.; Lelieveld, J. Modelling the global atmospheric transport and deposition of radionuclides from the Fukushima Dai-ichi nuclear accident. *Atmos. Chem. Phys.* **2013**, *13*, 1425–1438. [CrossRef]
31. Ten Hoeve, J.E.; Jacobson, M.Z. Worldwide health effects of the Fukushima Daiichi nuclear accident. *Energy Environ. Energy Environ. Sci.* **2012**, *9*, 8743–8757. [CrossRef]
32. Morino, Y.; Ohara, T.; Watanabe, M.; Hayashi, S.; Nishizawa, M. Episode analysis of deposition of radiocesium from the Fukushima Daiichi nuclear power plant accident. *Environ. Sci. Technol.* **2013**, *47*, 2314–2322. [CrossRef] [PubMed]
33. Kajino, M.; Sekiyama, T.T.; Igarshi, Y.; Katata, G.; Sawada, M.; Adachi, K.; Zaizen, Y.; Tsuruta, H.; Nakajima, T. Deposition and dispersion of radio-cesium released due to the Fukushima nuclear accident: Sensitivity to meteorological models and physical modules. *J. Geophys. Res. Atmos.* **2019**, *124*, 1823–1845. [CrossRef]
34. Bilgiç, E.; Gündüz, O. Analysis of the impact of various vertical release patterns on the atmospheric dispersion and total deposition of 137Cs from Chernobyl Nuclear Power Plant accident. *Environ. Sci. Pollut. Res.* **2021**, *28*, 66864–66887. [CrossRef]
35. Grell, G.A.; Peckham, S.E.; Schmitz, R.; Mckeen, S.A.; Frost, G.; Skamarock, W.C. Fully coupled "online" chemistry within the WRF model. *Atmos. Environ.* **2005**, *39*, 6957–6975. [CrossRef]
36. Hu, X.; Li, D.; Huang, H.; Shen, S.; Bou-Zeid, E. Modeling and sensitivity analysis of transport and deposition of radionuclides from the Fukushima Dai-ichi accident. *Atmos. Chem. Phys.* **2014**, *14*, 11065–11092. [CrossRef]
37. Fang, S.; Zhuang, S.H.; Goto, D.; Hu, X.Y.; Li, S.; Huang, S.X. Coupled modeling of in- and below-cloud wet deposition for atmospheric 137Cs transport following the Fukushima Daiichi accident using WRF-Chem: A self-consistent evaluation of 25 scheme combinations. *Environ. Int.* **2022**, *158*, 106882. [CrossRef] [PubMed]
38. Zhuang, S.H.; Fang, S.; Goto, D.; Dong, X.W.; Xu, Y.H.; Sheng, L. Model behavior regarding in- and below-cloud 137Cs wet scavenging following the Fukushima accident using 1-km-resolution meteorological field data. *Sci. Total Environ.* **2023**, *872*, 162165. [CrossRef] [PubMed]

39. Povinec, P.P.; Gera, M.; Holý, K.; Hirose, K.; Lujanienė, G.; Nakano, M.; Plastino, W.; Sýkora, I.; Bartok, J.; Gažák, M. Dispersion of Fukushima radionuclides in the global atmosphere and the ocean. *Appl. Radiat. Isot.* **2013**, *81*, 383–392. [CrossRef]
40. Fei, J.F.; Wang, P.F.; Cheng, X.P.; Huang, X.G.; Wang, Y.B. A regional simulation study on dispersion of nuclear pollution from the damaged Fukushima Nuclear Power Plant. *Sci. China Earth Sci.* **2014**, *57*, 1513–1524. [CrossRef]
41. Jiang, F.; Wang, T.J.; Wang, T.T.; Xie, M.; Zhao, H. Numerical modeling of a continuous photochemical pollution episode in Hong Kong using WRF-Chem. *Atmos. Environ.* **2008**, *38*, 8717–8727. [CrossRef]
42. Veefkind, J.P.; Aben, I.; McMullan, K.; Förster, H.; de Vries, J.; Otter, G.; Claas, J.; Eskes, H.J.; de Haan, J.F.; Kleipool, Q.; et al. TROPOMI on the ESA Sentinel-5 Precursor: A GMES mission for global observations of the atmospheric composition for climate, air quality and ozone layer applications. *Remote Sens. Environ.* **2012**, *120*, 70–83. [CrossRef]
43. Mlawer, E.J.; Taubman, S.J.; Brown, P.D.; Iacono, M.J.; Clough, S.A. Radiative transfer for inhomogeneous atmospheres: RRTM, a validated correlated-k model for the longwave. *J. Geophys. Res.* **1997**, *102*, 16663–16682. [CrossRef]
44. Dudhia, J. Numerical Study of Convection Observed during the Winter Monsoon Experiment Using a Mesoscale Two-Dimensional Model. *J. Atmos. Sci.* **1989**, *46*, 3077–3107. [CrossRef]
45. Chen, Y.Y.; Yang, K.; Zhou, D.G.; Qin, J.; Guo, X.F. Improving the Noah Land Surface Model in Arid Regions with an Appropriate Parameterization of the Thermal Roughness Length. *J. Hydrometeorol.* **2010**, *11*, 995–1006. [CrossRef]
46. Janjic, Z.I. The step-mountain eta coordinate model: Further developments of the convection, viscous sublayer, and turbulence closure schemes. *Mon. Weather Rev.* **1994**, *122*, 5. [CrossRef]
47. Grell, G.A.; Dévényi, D. A generalized approach to parameterizing convection combining ensemble and data assimilation techniques. *Geophys. Res. Lett.* **2002**, *29*, 38-1–38-4. [CrossRef]
48. Grell, G.A. Prognostic evaluation of assumptions used by cumulus parameterizations. *Mon. Weather Rev.* **1993**, *121*, 764–787. [CrossRef]
49. Baklanov, A.A.; Sørensen, J.H. Parameterisation of radionuclide deposition in atmospheric long-range transport modelling. *Phys. Chem. Earth Part B Hydrol. Ocean. Atmos.* **2001**, *26*, 787–799. [CrossRef]